

Reversible shuffle twinning yields anisotropic tensile superelasticity in ceramic GeSe

Received: 10 August 2024

Accepted: 12 March 2025

Published online: 10 April 2025

 Check for updates

Chong Wang^{1,5}, Zeya Li^{2,3,5}, Yingchun Cheng^{1,5}, Xiao-Ji Weng¹✉, Yeqiang Bu⁴, Kun Zhai¹, Tianyu Xue¹, Hongtao Yuan^{2,3}✉, Anmin Nie¹✉, Xiang-Feng Zhou¹, Hongtao Wang⁴, Yongjun Tian¹ & Zhongyuan Liu¹

Superelasticity is a reversible, nonlinear strain response to stress stimuli beyond the linear elastic regime. It is commonly associated with a martensitic transformation in its host material, usually a metal or polymer. Except for the ceramic crystals ZrO_2 and BaTiO_3 , which show superelasticity under compressive stress, inorganic materials with covalent or ionic bonding usually do not exhibit superelastic behaviour because of large energy barriers for structural transitions. Here we show anisotropic tensile superelasticity in the ceramic crystal GeSe, which originates from reversible shuffle twinning. Through in situ transmission electron microscopy mechanical testing, we trace the evolution from a linear elastic behaviour to a nonlinear superelastic plateau in stress–strain curves and concurrently observe the generation of stripy-shaped twin domains along the $\langle 110 \rangle$ direction. Density functional theory calculations paired with molecular dynamics simulations reveal a release of elastic potential energy upon the shuffle twinning process from a Z-shaped to an anti-Z-shaped bond configuration, which is responsible for the observed tensile superelasticity. This mechanism makes the observed superelasticity highly directional. In line with the anisotropic Young's modulus and Poisson's ratio in GeSe, experiments confirm that superelastic response emerges only when we apply strain along or close to the zigzag direction. We expect to find similar anisotropic superelasticity in ceramic semiconductors with similar crystal structure such as SnSe, SnS or GeS.

Large capability of superelastic deformation in structural materials is desirable for practical mechanical devices and flexible electronics^{1–5}. Unlike the non-directional and delocalized metallic bonds, which can easily drive the displacive movement of atoms for structural transition in metals and thus realize superelasticity with large deformation therein (Fig. 1a), the directional and saturated nature of chemical bonds in inorganic non-metallic materials typically hinders such structural transitions and is not expected to facilitate superelasticity^{6–10}. In ceramic

crystals, the interaction between neighbouring atoms dominated by repulsion at short distances and attraction at long distances (similar to the Lennard-Jones potential^{11,12} shown in Fig. 1b) plays an important role in their elastic mechanical properties. Owing to the strong asymmetry of the Lennard-Jones potential curve far from the equilibrium position (the potential quickly diverges with atoms getting closer while slowly saturating to zero potential energy with atoms getting farther apart), the atom interactions shown in the Lennard-Jones potential behave in

A full list of affiliations appears at the end of the paper. ✉e-mail: xjweng@ysu.edu.cn; htyuan@nju.edu.cn; anmin@ysu.edu.cn

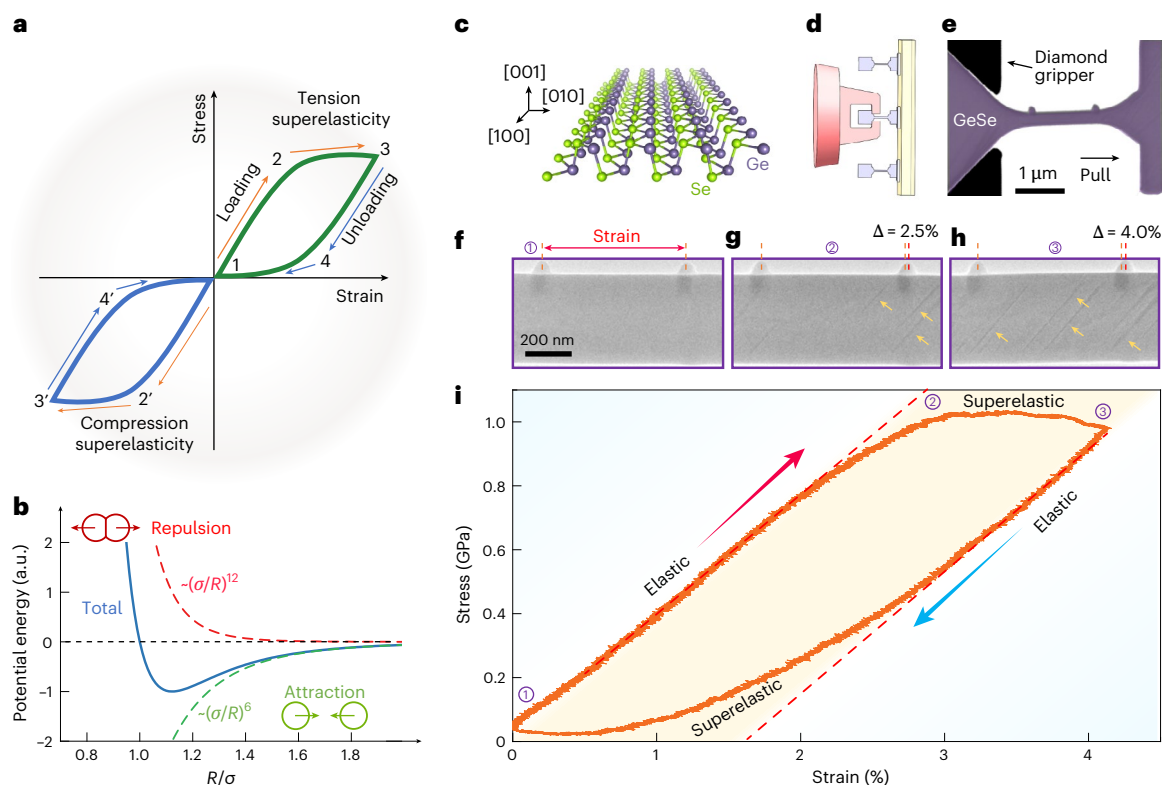


Fig. 1 | Observation of emergent superelasticity in ceramic crystal GeSe. **a**, Schematic of the stress-strain relationship for tensile and compressive superelastic deformations during the loading and unloading process. **b**, Schematic illustration of the interatomic potential as a function of atom distance. Here R denotes the distance between two interacting atoms, while σ represents the distance at which the potential energy equals zero. **c**, Crystal structure of GeSe (space group $Pnma$) viewed along the [100] direction. The purple and green balls represent Ge and Se atoms, respectively. **d**, Schematic

diagram for the in situ uniaxial tensile equipment via the DT method. **e**, TEM image of GeSe nanobridges and diamond tensile gripper for the tensile test. **f-h**, In situ TEM images of the GeSe sample (sample A) before loading (f), at the beginning of superelasticity emergence (g) and at the maximum load (h). **i**, Stress-strain curve of a typical GeSe sample measured via the DT method. The critical strain for the emergence of superelasticity is roughly determined as the intersection of the tangent lines of the data in the linear elastic region and superelastic plateau region.

different ways under tension and compression limits¹³, respectively, thus leading to variations between tensile and compressed superelasticity¹⁴. Although superelasticity under compressive stress has been observed in two specific ceramic crystals (ZrO_2 and BaTiO_3)^{15–17}, tensile superelasticity has not been observed in ceramic crystals.

GeSe is a layered ceramic crystal and possesses unique structural and bonding characteristics: (1) its puckered orthorhombic lattice (Fig. 1c and Extended Data Fig. 1) enables notable elastic deformation under low stress^{18,19}, (2) its in-plane anisotropy creates distinct mechanical properties along the zigzag and armchair directions²⁰, and (3) its metavalent bonding, which lies between metallic and covalent bonds, provides a balance of mechanical flexibility and electronic functionality^{21–23}. These features make GeSe an ideal candidate for exploring tensile superelasticity in ceramics.

In this work, we demonstrate directional tensile superelasticity in GeSe. With in situ mechanical high-resolution transmission electron microscopy (HRTEM), we unveil the stress-strain response; the linear elastic behaviour evolves into a superelastic plateau at a critical strain, which is accompanied by the simultaneous generation of stripy-shaped twin domains along the $\langle 110 \rangle$ orientation. These stripy-shaped twin domains grow rapidly in width with a further increase in strain. Notably, the twinning-driven superelasticity is anisotropic and only emerges at strain angles close to the zigzag direction. First-principles calculations reveal that the shuffle twinning process, which is based on the bond-configuration change from Z-shape to anti-Z-shape, leads to a release of elastic potential energy in GeSe and yields superelastic behaviour. This anisotropic mechanism for achieving superelasticity is

distinct from the common martensitic transformation mechanism for superelasticity in metals. Our findings not only establish an alternative mechanism for achieving tensile superelasticity in ceramic crystals but also offer opportunities for designing advanced semiconductor materials with tailored mechanical properties, for example, for integration into flexible electronics or mechanical systems.

Superelasticity in GeSe ceramic crystal

We prepared GeSe samples and conducted in situ TEM tensile measurements using push-to-pull (PTP)²⁴ and direct-tensile (DT)²⁵ methods (Methods, Fig. 1d,e, Extended Data Fig. 2 and Supplementary Fig. 1). Figure 1i shows the stress-strain curve for a typical DT sample (150 nm thick), where the stress-strain responses and TEM images (Fig. 1f–h) were collected simultaneously with stress applied along the zigzag direction, as further illustrated by in situ dark-field TEM images in Supplementary Fig. 2. In Fig. 1i, the GeSe sample initially shows linear elastic behaviour, transitioning to near-plateau stress behaviour when the strain exceeds 2.5% (Supplementary Fig. 3). Simultaneously, certain stripy domains emerge, as shown by TEM images, forming only at specific angles ($47^\circ \pm 2^\circ$ or $133^\circ \pm 2^\circ$) relative to the zigzag direction (Extended Data Fig. 3 and Supplementary Table 1), which implies that the domain boundaries prefer to form along certain high-symmetric crystallographic directions. Consistent with the superelastic loop, both the emergence and the disappearance of stripy domains can be confirmed with strain loading and unloading (Fig. 1f–h, Supplementary Fig. 2 and Supplementary Videos 1–3). The occurrence of superelasticity in GeSe is influenced by sample dimensions and strain

rate (Supplementary Figs. 4–6). However, the reversible stripy twin domains and consistent critical strain ($\sim 2.5\%$) are highly reproducible, confirmed in over 44 GeSe samples (Supplementary Figs. 3, 7 and 8, and Supplementary Table 1). Since such a loop-shaped stress–strain curve is always regarded as the typical behaviour for superelasticity, which has been widely observed in those superelastic metallic alloys driven by martensitic transformation^{3,10}, these results might indicate that the superelastic behaviour in GeSe ceramic crystal is microscopically associated with the reversible formation of stripy domains.

Reversible shuffle twinning mechanism

To investigate the microscopic formation of superelasticity in GeSe ceramic crystal, we performed *in situ* HRTEM imaging on PTP samples to examine the evolution of atomic domain structures under strain (Fig. 2a–c, Extended Data Fig. 4, Supplementary Fig. 1b and Supplementary Videos 4 and 5). Figure 2a–c, along with Supplementary Video 4, shows a sample viewed along the *c* direction during loading in the zigzag direction of GeSe. By contrast, Extended Data Fig. 4 and Supplementary Video 5 depict another sample viewed along the armchair direction during loading (Supplementary Fig. 1b). Figure 2a shows four stages during the evolution of stripy domain with strain loading: (1) the stripy domain emerges at 69 s, coinciding with the transition of the stress–strain curve to superelastic behaviour; (2) the stripy domain grows to ~ 15 nm in width by 105 s, corresponding to the nonlinear superelastic regime; (3) during strain unloading (105–123 s), the domain width remains unchanged owing to the recovery of the linear elastic strain; (4) after full strain release, the domain narrows and disappears, resulting in nonlinear superelastic recovery (Supplementary Fig. 9). This reversible formation and disappearance of stripy domains underlie the superelastic loop behaviour in GeSe ceramic crystal.

To confirm the crystal structure of newly formed stripy domains, we performed fast Fourier transform (FFT) analysis for the matrix and stripy domain region in HRTEM images. As shown in Fig. 2b,c, the stripy domain shares the same crystal structure and lattice symmetry as the matrix, with their zigzag directions rotated by 82.5° relative to each other. The stripy twin domain is connected to the matrix region through highly coherent interfaces, with twin boundaries oriented along the $\langle 110 \rangle$ direction of the matrix, as revealed by atomic-scale high-angle annular dark-field scanning transmission electron microscopy (HAADF-STEM) images (Fig. 2d–f, Extended Data Fig. 5 and Supplementary Fig. 10). This evidence confirms that the superelasticity in GeSe ceramic crystal originates from reversible twinning processes rather than phase transformations. Interestingly, twins tend to nucleate at locations with high stress concentrations, such as surfaces and local defects (Supplementary Fig. 11). This twinning process can serve as an alternative mechanism to generate the superelasticity in ceramic crystals, distinct from the martensitic-transformation-driven superelasticity in shape memory alloys^{3,10}.

We performed *ab initio* total energy calculations to understand the energetically favourable twinning crystal structures under varying tensile strains (Fig. 2g). Two key points are highlighted in Fig. 2g. First, the twin structure becomes more stable at larger strains, as shown by the notable reduction of final state energy with increasing strain (Fig. 2h). The relative energy of the final state to the initial state decreases to a negative value as the strain reaches 7%, indicating that such a strain drives twin structure formation. Second, twinning under strain can occur spontaneously even at room temperature as the energy barrier for twinning decreases to below 5 meV per atom with increasing strain. This ultralow barrier suggests that even mild exothermic reactions under large strain can drive twin domain formation, enabling an easy route to superelasticity.

As shown in the cartoon atomic configuration in the inset of Fig. 2g and Extended Data Fig. 6a,b, the spontaneous twinning process microscopically arises from changing between the Z-shaped and anti-Z-shaped atomic configurations along the $[110]$ direction.

As the in-plane Ge¹–Se¹ bond stretches under tensile strain and the surrounding non-bonded Ge and Se atoms (for example, Ge¹–Se²) move closer, the strain eventually breaks the Ge¹–Se¹ bond and forms a new Ge¹–Se² bond (Fig. 2g and Supplementary Fig. 12). This twinning process, induced by Z-shaped to anti-Z-shaped bond switching, involves the collective rotation of Ge–Se atom pairs arranged in the $[110]$ direction and can be regarded as the shuffle twinning process. The bond-switching-mediated twinning processes in GeSe occur at a much lower energy cost compared with slip-induced stacking fault mechanism (Supplementary Fig. 13). In contrast to the abrupt atom rearrangement in structural transitions, the uniform atomic shuffling in typical twinning processes can always introduce fewer lattice defects and lower residual stress in materials, considerably reducing the risk of material failure and cracking^{26,27}.

To understand the twin formation dynamics in GeSe ceramic crystal, we performed *ab initio* molecular dynamics (AIMD) simulations under uniaxial strain (Methods, Fig. 3a–c, Supplementary Figs. 14–16 and Supplementary Video 6). Figure 3b,c shows the stress–strain and the energy–strain curves from the AIMD simulations. The simulations revealed that once a Ge–Se atom pair rotates to drive Z-shaped to anti-Z-shaped bond switching, it promotes the rotation of adjacent pairs, rapidly forming and growing twin domains within an ultrafast picosecond timeframe (Fig. 3a). Correspondingly, the energy–strain curve of twinning GeSe deviates dramatically from the expected elastic behaviour of untwined GeSe, with the calculated energy of the twin domain structure being much lower (Fig. 3b). This indicates that twin domain formation reduces the elastic energy, making twinning and nonlinear superelasticity feasible under strain. In addition, we confirmed that the formation of new twin domains causes a stress drop in the stress–strain curve, demonstrating that the required stress for a target strain is substantially reduced after twinning. This demonstrates that twin domain formation is the dominant mechanism for the nonlinear deformation in GeSe ceramic crystal. For example, Fig. 3b,c and Extended Data Fig. 6c show that stress and energy drops occur at 6% and 9% strain owing to the formation of new twin domains, which release elastic energy and drive nonlinear superelastic behaviour during loading. In the calculation, twins may form at higher strains, possibly owing to model size limitations that overestimate twin proportions. Our AIMD simulations, consistent with experimental observations, confirmed that the reversible shuffle twinning process drives superelasticity. Interestingly, the shuffle twinning mechanism and resulting twin domains were also experimentally observed in sulfide-based GeS ceramic crystals with the same puckered structure (Extended Data Fig. 7), suggesting that this mechanism could be a universal strategy for inducing superelasticity in other ceramic crystals.

Lattice evolution during superelastic deformation

To better understand the superelastic behaviour in GeSe crystal at the atomic scale, we extracted in-plane lattice parameters from HRTEM images and analysed their evolution during the strain loading–unloading process (Fig. 3d–f, Extended Data Fig. 8, Supplementary Fig. 17, Supplementary Table 2 and Supplementary Video 7). Consistent with the discussion above, the in-plane lattice strain evolution in each cycle can be divided into four regions, including two linear regions during initial loading (L1) and unloading (L2) and two superelastic regions during loading (S1) and unloading (S2). In region S1, after the critical strain for twin domain formation, the lattice parameter along the armchair direction of the twin domain is stretched (owing to a twinning angle of $\sim 82.5^\circ$), and the lattice strain dramatically increases to 5.8% with rapid twin domain growth, while the matrix lattice strain along the zigzag direction decreases from 2% to 1%. Interestingly, the formation and rapid growth of twin domains enhance the GeSe deformation, resulting in observed superelasticity along the matrix zigzag direction, as the lattice parameter along the armchair direction ($b = 4.38$ Å) is much larger than that along the zigzag direction ($a = 3.81$ Å). On the basis of

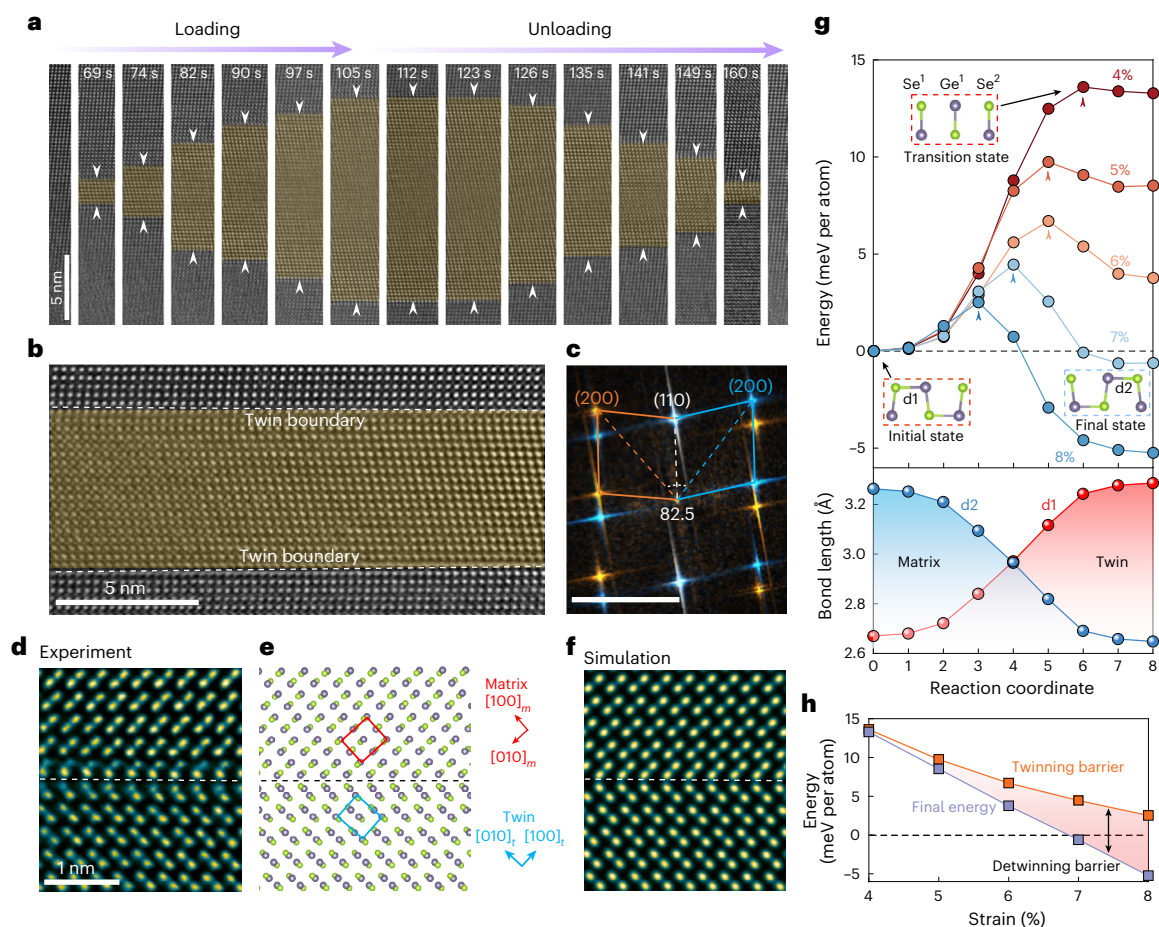


Fig. 2 | Evolution of the stripy twin domain in GeSe under tensile loading and unloading strains. **a**, High-resolution TEM snapshots taken along the $\langle 001 \rangle$ zone axis of the GeSe sample (sample B) under the loading and unloading strains. **b, c**, The FFT pattern (**c**) of the HRTEM image (**b**) corresponding to the region containing a twin domain. The scale bar in the FFT pattern is 5 nm^{-1} . **d–f**, HAADF-STEM image (**d**), corresponding structural model (**e**) and simulated HAADF-STEM image (**f**) of a twin boundary. Here HRTEM and HAADF-STEM images of sample B, obtained via the PTP method, reveal twinning behaviour in the first cycle and atomic-resolution details of twinning structure formed in the subsequent cycle.

the sample's modulus and measured lattice strain, we estimated the stress–strain curves, which exhibit a clear hysteresis feature (Supplementary Fig. 18) and align well with those obtained via DT testing. Notably, the lattice parameter evolution and lattice strain behaviour in both the first and second cycles are nearly identical, demonstrating excellent recyclability of GeSe's superelastic behaviour.

Generally, the maximum strain ϵ_{max} can be estimated by the following formula:

$$\epsilon_{\text{max}} = \frac{xb(1 + \epsilon_{\text{max}}^{\text{ac}}) + (1 - x)a(1 + \epsilon_{\text{max}}^{\text{zz}})}{a} - 1$$

where $\epsilon_{\text{max}}^{\text{ac}}$ and $\epsilon_{\text{max}}^{\text{zz}}$ are the maximum local strains that can be reached before the fracture along the armchair and zigzag directions (Supplementary Fig. 19), and x is the proportion of the matrix that has transformed into twin domains. a and b refer to the lattice parameters of GeSe, with values of 3.81 \AA and 4.38 \AA , respectively. According to the local lattice strain analysis in Fig. 3e, the observed largest values of $\epsilon_{\text{max}}^{\text{ac}}$ and $\epsilon_{\text{max}}^{\text{zz}}$ can be estimated to be -5.8% and -2.9% , respectively. Assuming that half of the matrix transforms into twin domains ($x = 0.5$), the maximum strain is theoretically -12.3% . Experimentally, with stripy

g, Top: the energy profile of the twinning transformation pathway at different strain values. Arrows indicate the energy saddle points. The inset schematic illustrates the bond breakage and formation during twinning/detwinning in GeSe under uniaxial strain along the zigzag direction. Here the energy of the initial state is set as zero energy. Bottom: the corresponding distance changes of $\text{Ge}^{\text{I}}\text{--Se}^{\text{I}}$ and $\text{Ge}^{\text{I}}\text{--Se}^{\text{II}}$ atoms during the twinning process. d_1 and d_2 represent the bond lengths of $\text{Ge}^{\text{I}}\text{--Se}^{\text{I}}$ and $\text{Ge}^{\text{I}}\text{--Se}^{\text{II}}$, respectively. The bond length for GeSe without strain is calculated to be 2.60 \AA . **h**, The final energy, twinning barrier and detwinning barrier as a function of strain.

domain formation, a maximum strain of -12.8% is achieved before GeSe sample fracture (Extended Data Fig. 9), aligning well with theoretical predictions. Twinning elements²⁶ obtained from HRTEM show a twinning shear of -0.30 , also consistent with theoretical estimates (Supplementary Fig. 20). Although twinning shear may cause localized nonuniform deformation, this deformation recovers after unloading (Supplementary Fig. 21) if no cracking occurs within the twin domain (Supplementary Fig. 22 and Supplementary Video 8). Compared with other layered materials, GeSe's small Young's modulus and twinning-induced superelasticity enable a large strain limit (Supplementary Fig. 23 and Supplementary Table 3), offering great potential for advanced mechanical applications^{28–30}. In addition, compared with other well-known superelastic materials, GeSe offers unique features such as a large strain limit, excellent cyclability (Supplementary Figs. 24 and 25, Supplementary Table 4 and Supplementary Video 9), an alternative superelastic mechanism and its distinctive two-dimensional semiconductor properties.

Directional superelasticity

To confirm the stress directions exhibiting the superelasticity in GeSe, we performed the tensile–strain measurements based on PTP samples

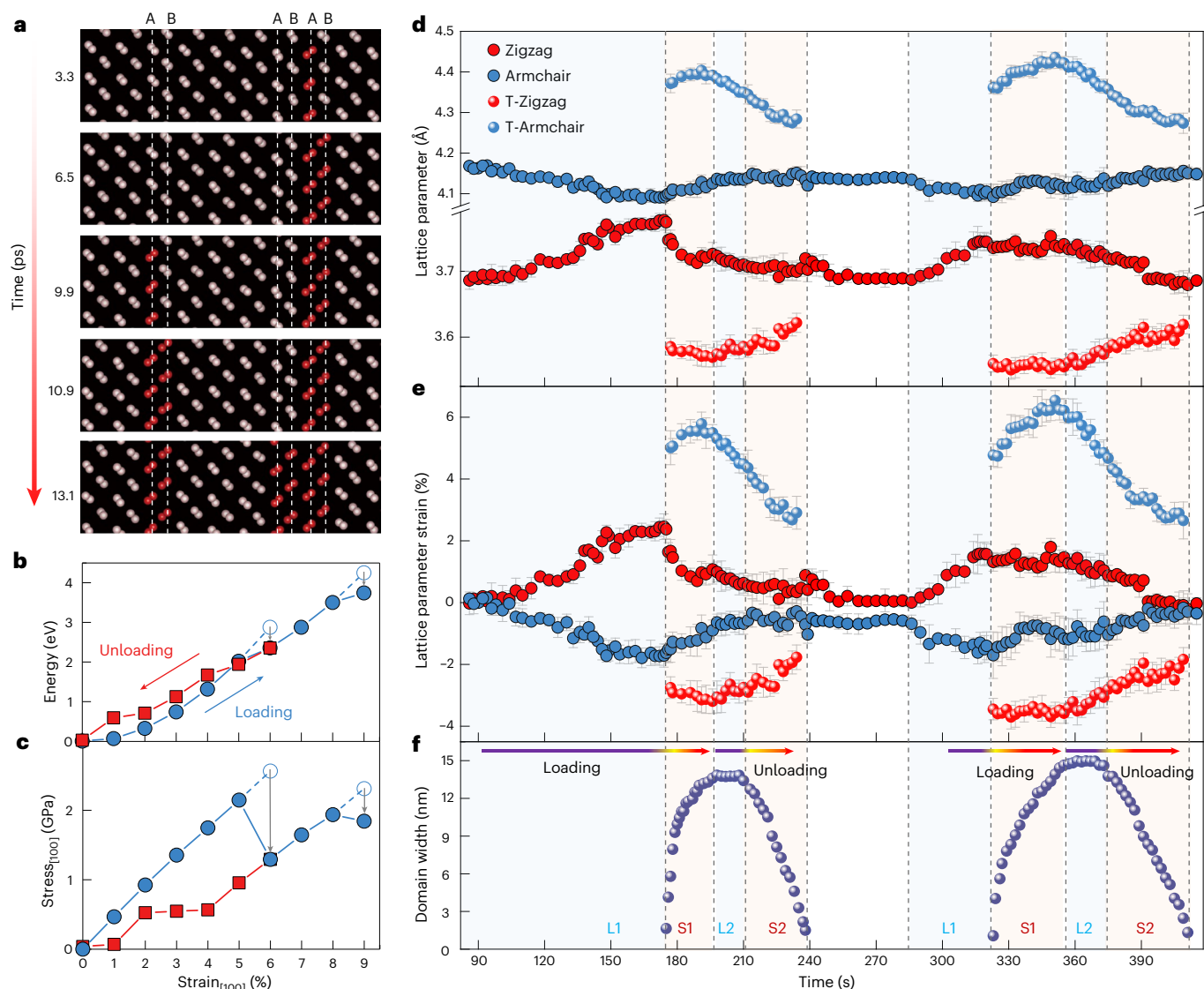


Fig. 3 | Local lattice strain analysis of GeSe under tensile strain loading–unloading. **a**, Statistical averages of the structure in different time intervals for the molecular dynamics of GeSe under 6% strain along the [100] direction. AB represents the stacking sequence of the original lattice. The model images cross 32 primitive cells of GeSe. **b**, Calculated energy of GeSe as a function of strain along the zigzag direction. **c**, Simulated stress–strain curve of GeSe as a function of strain along the zigzag direction. **d–f**, Evolution of the stripy domain width (**f**), in-plane lattice parameters (**d**) and derived local in-plane lattice strains in the matrix and stripy domain (**e**) during the loading–unloading tensile strains of sample C obtained using the PTP method. The local lattice strain is derived by $\varepsilon = \Delta L/L$, where L is the lattice parameter along the zigzag or armchair direction

and ΔL is the corresponding change of lattice parameter under stress. In the first loading–unloading cycle, loading and unloading begin at 86 s and 200 s, respectively, while in the second cycle, loading and unloading begin at 285 s and 356 s, respectively. L1 and S1 indicate the linear elastic stage and the nonlinear superplastic stage during loading, respectively, while L2 and S2 represent the linear elastic stage and the nonlinear superplastic stage during unloading. The two loading–unloading cycles are extracted from Supplementary Video 7. Here the HRTEM dataset from the first and second cycles of sample C, obtained using the PTP method, highlights the evolution of lattice parameters across multiple cycles, complementing the data in Fig. 2.

with the bridge oriented at different angles (θ , the angle between the zigzag and loading directions). Unlike the superelastic behaviour observed under strain along the zigzag direction, GeSe samples subjected to strain along the armchair direction show only reversible linear elastic behaviour, without stripy domain formations, before fracturing at ~5% strain (Supplementary Fig. 26). This suggests that GeSe superelasticity is highly dependent on the loading direction. Figure 4a shows in situ TEM images of PTP samples with θ ranging from 0° to 180° (Extended Data Fig. 10). Observable stripy domains (indicative of superelasticity) appear only when θ is between 325° and 30° (or 145° and 210°). At all other angles, no stripy domains are observed, even when samples are stretched to fracture. Young's modulus of GeSe along the armchair direction is ~27 GPa, much smaller than that along the zigzag

direction (~40 GPa), suggesting that this anisotropic Young's modulus may underlie the directional superelasticity in GeSe³¹.

We calculated Young's modulus of the matrix and twin domains along specific tensile directions. As shown in Fig. 4b, the angle-dependent Young's modulus shows strong anisotropy along zigzag and armchair directions, consistent with the experimental results. Twinning generally occurs during the loading to release elastic energy, but only when the matrix's Young's modulus greatly exceeds that of the twin domain, as observed for loading directions near the zigzag direction (Supplementary Fig. 28). To achieve the transition state in Fig. 2g and interchange the zigzag and armchair directions of GeSe, the loading direction must enable convergence of lattice lengths a and b . The calculated Poisson's ratio decreases from +1.13 along the zigzag

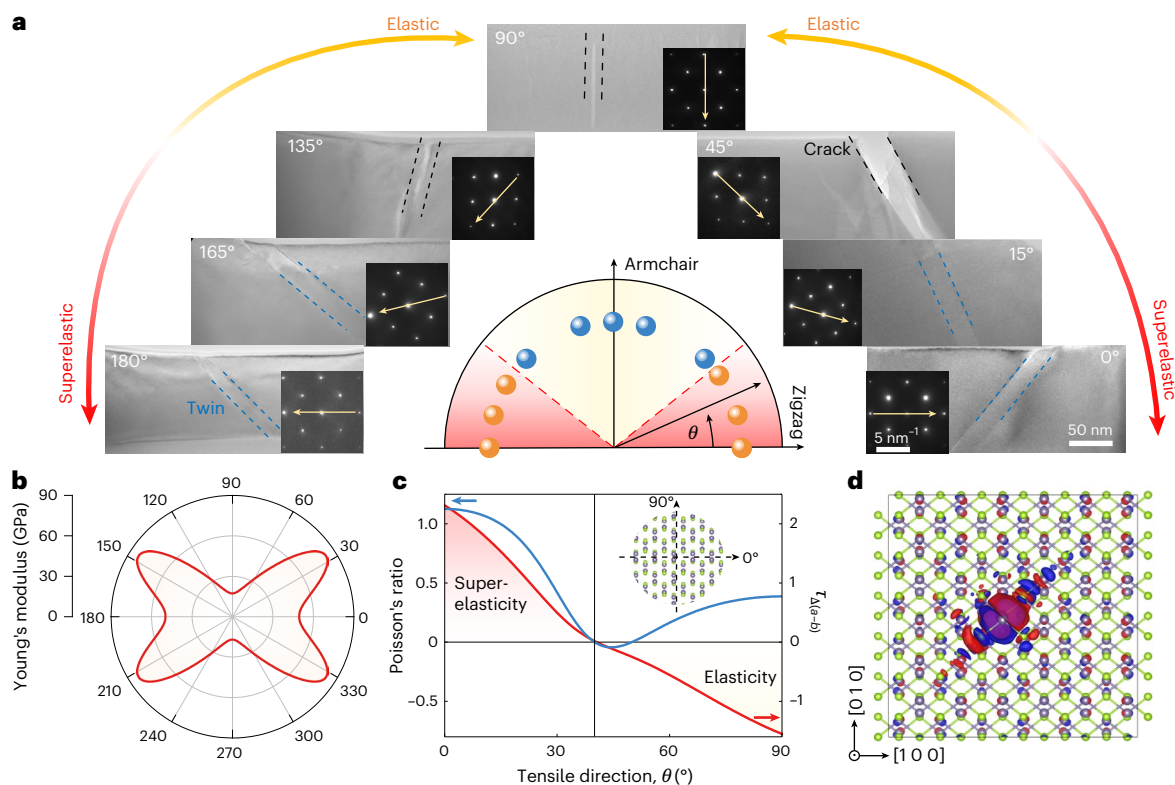


Fig. 4 | Directional superelasticity in GeSe ceramic crystal. a, Loading direction dependence of superelasticity in GeSe. TEM images showing typical fabricated GeSe samples for PTP testing, featuring different bridge orientations with respect to the zigzag direction. Insets: SAED patterns of the tested samples. The zigzag direction of each sample is indexed by a red arrow, and the stripy domains generated owing to tensile strain are highlighted by blue dashed lines. The black dashed lines indicate the fracture of the tested samples under a large strain. Middle inset: schematic diagram illustrating the range of tensile directions for the appearance of superelasticity in GeSe. The balls represent the experimentally measured values of θ , among which the orange balls highlight the superelastic

case and the blue balls highlight the elastic case. **b**, The calculated Young's modulus of GeSe along different directions. Angle of 0° indicates the strain along the zigzag ([100]) direction. **c**, Poisson's ratio and convergence coefficient τ along different directions. τ indicates the ease of convergence between a and b with axial tensile strain. Inset: the orientation of GeSe crystal. **d**, Top view of charge density difference between a GeSe structure with one Ge–Se pair rotated by 90° and one without bond rotation. Ge and Se atoms are coloured in purple and green, respectively. The red and blue bubbles indicate the increase and decrease of the charge density, corresponding to the electron dissipation and collection, respectively.

direction ($\theta = 0$) to negative values in the interval $40^\circ < \theta < 50^\circ$, and then increases to $+0.39$ along the armchair direction (Fig. 4c and Supplementary Fig. 27). A convergence coefficient τ , related to Poisson's ratio, indicates the ease of convergence between a and b (Supplementary equation (7)). τ decreases as θ increases, and convergence occurs only when τ is positive—the higher the value, the easier the convergence. Thus, a approaches b most rapidly at $\theta = 0$, but slows and is inhibited as θ increases (Fig. 4c, details in Supplementary Information). These calculations align with experimental observations, where twinning and superelasticity occur under tensile loading at $\theta < 40^\circ$.

To understand the relationship between directional Ge–Se bonds and the twin domain (observed in Figs. 1f–h and 4a), we calculated the charge density difference between a GeSe structure with one Ge–Se pair rotated by 90° and one without rotation (Fig. 4d). Rotating a single Ge–Se pair causes a considerable perturbation in the charge density, more pronounced along the [110] direction than [100] and [010] directions. This large charge perturbation destabilizes the local electron structure, prompting bond reconstruction. When an adjacent Ge–Se pair along the [110] direction rotates owing to this perturbation, the effect propagates further along the same direction. This agrees with MD simulation (Supplementary Video 6), which shows that shuffle twinning rapidly originates from a single Ge–Se pair rotation. It also explains the fast nucleation and growth of twins along the [110] direction in experiments. Therefore, directional bonding plays an important role in the formation of directional twin domains in GeSe, providing a

platform to modulate the mechanical properties of ceramic crystals (Supplementary Fig. 29).

Conclusion

We observed anisotropic tensile superelasticity in ceramic crystal GeSe. The underlying reversible shuffle twinning mechanism, which is distinct from the structural transition-driven superelasticity in metallic alloys, may be also operational in other ceramic semiconductors with similar crystal structures^{32,33}, including but not limited to SnSe, SnS, GeS and their doped counterparts (Supplementary Figs. 30 and 31 and Supplementary Tables 5 and 6). Mechanical-stimuli-driven ferroelasticity has been demonstrated in chalcogenides³⁴, and intrinsic ferroelectricity is known in structurally analogous materials^{35,36}. The discovery of tensile superelasticity in GeSe raises hope for coexisting ferroelastic, ferroelectric and superelastic behaviour in this material class—a multifunctional coupling mechanism analogous to domain-engineered functionalities in BiFeO₃, where twin boundaries host emergent properties such as interfacial conductivity and photovoltaic effects^{37,38}. While experimental evidence of this interplay in GeSe is still lacking, the strain-dependent twinning–detwinning process, combined with chalcogenides' spin helicity³⁹, nonlinear optics⁴⁰ and bulk photovoltaic effects^{41,42}, provides a promising starting point for the development of strain-modulated optoelectronics. For example, mechanically responsive devices, such as photodetectors or sensors, could utilize strain-induced electronic state modifications, similar to domain-wall-enabled functionalities

in BiFeO₃. With further advances in heterostructure engineering and localized property characterization, these concepts could be translated into practical applications. Texture engineering and doping strategies together with the extension beyond single-crystal GeSe to polycrystalline materials or other ceramics with different bonding characteristics could help broaden the scope for potential applications of anisotropic tensile superelasticity.

Online content

Any methods, additional references, Nature Portfolio reporting summaries, source data, extended data, supplementary information, acknowledgements, peer review information; details of author contributions and competing interests; and statements of data and code availability are available at <https://doi.org/10.1038/s41565-025-01902-7>.

References

- He, Q. F. et al. A highly distorted ultraelastic chemically complex Elinvar alloy. *Nature* **602**, 251–257 (2022).
- Pang, E. L., Olson, G. B. & Schuh, C. A. Low-hysteresis shape-memory ceramics designed by multimode modelling. *Nature* **610**, 491–495 (2022).
- Omori, T. et al. Superelastic effect in polycrystalline ferrous alloys. *Science* **333**, 68–71 (2011).
- Schaedler, T. A. et al. Ultralight metallic microlattices. *Science* **334**, 962–965 (2011).
- Meza, L. R., Das, S. & Greer, J. R. Strong, lightweight, and recoverable three-dimensional ceramic nanolattices. *Science* **345**, 1322–1326 (2014).
- Bhattacharya, K., Conti, S., Zanzotto, G. & Zimmer, J. Crystal symmetry and the reversibility of martensitic transformations. *Nature* **428**, 55–59 (2004).
- Chen, H. et al. Unprecedented non-hysteretic superelasticity of [001]-oriented NiCoFeGa single crystals. *Nat. Mater.* **19**, 712–718 (2020).
- Juan, J. S., Nó, M. L. & Schuh, C. A. Nanoscale shape-memory alloys for ultrahigh mechanical damping. *Nat. Nanotechnol.* **4**, 415–419 (2009).
- Gómez-Cortés, J. F. et al. Size effect and scaling power-law for superelasticity in shape-memory alloys at the nanoscale. *Nat. Nanotechnol.* **12**, 790–796 (2017).
- Tanaka, Y. et al. Ferrous polycrystalline shape-memory alloy showing huge superelasticity. *Science* **327**, 1488–1490 (2010).
- Jones, J. E., Ingham, A. E. & Chapman, S. On the calculation of certain crystal potential constants, and on the cubic crystal of least potential energy. *Proc. R. Soc. A* **107**, 636–653 (1997).
- Schwerdtfeger, P. & Wales, D. J. 100 years of the Lennard-Jones potential. *J. Chem. Theory Comput.* **20**, 3379–3405 (2024).
- Wang, Y. et al. Tension–compression asymmetry in amorphous silicon. *Nat. Mater.* **20**, 1371–1377 (2021).
- Panchenko, E., Chumlyakov, Y., Maier, H. J., Timofeeva, E. & Karaman, I. Tension/compression asymmetry of functional properties in [001]-oriented ferromagnetic NiFeGaCo single crystals. *Intermetallics* **18**, 2458–2463 (2010).
- Dong, G. et al. Super-elastic ferroelectric single-crystal membrane with continuous electric dipole rotation. *Science* **366**, 475–479 (2019).
- Lai, A., Du, Z., Gan, C. L. & Schuh, C. A. Shape memory and superelastic ceramics at small scales. *Science* **341**, 1505–1508 (2013).
- Li, Y. et al. Superelastic oxide micropillars enabled by surface tension–modulated 90° domain switching with excellent fatigue resistance. *PNAS* **118**, e2025255118 (2021).
- Gomes, L. C., Carvalho, A. & Castro Neto, A. H. Enhanced piezoelectricity and modified dielectric screening of two-dimensional group-IV monochalcogenides. *Phys. Rev. B* **92**, 214103 (2015).
- Wei, Q. & Peng, X. Superior mechanical flexibility of phosphorene and few-layer black phosphorus. *Appl. Phys. Lett.* **104**, 251915 (2014).
- Guan, Z. et al. Electric-field-induced room-temperature antiferroelectric–ferroelectric phase transition in van der Waals layered GeSe. *ACS Nano* **16**, 1308–1317 (2022).
- Lucovsky, G. & White, R. M. Effects of resonance bonding on the properties of crystalline and amorphous semiconductors. *Phys. Rev. B* **8**, 660–667 (1973).
- Shportko, K. et al. Resonant bonding in crystalline phase-change materials. *Nat. Mater.* **7**, 653–658 (2008).
- Guarneri, L. et al. Metavalent bonding in crystalline solids: how does it collapse? *Adv. Mater.* **33**, 2102356 (2021).
- Lin, W. T. et al. Highly pressurized helium nanobubbles promote stacking-fault-mediated deformation in FeNiCoCr high-entropy alloy. *Acta Mater.* **210**, 116843 (2021).
- Dang, C. et al. Achieving large uniform tensile elasticity in microfabricated diamond. *Science* **371**, 76–78 (2021).
- Bilby, B. A., Crocker, A. G. & Cottrell, A. H. The theory of the crystallography of deformation twinning. *Proc. R. Soc. A* **288**, 240–255 (1997).
- Hannink, R. H. J., Kelly, P. M., & Muddle, B. C. Transformation toughening in zirconia-containing ceramics. *J. Am. Ceram. Soc.* **83**, 461–487 (2000).
- Kim, D. H. et al. Ultrathin silicon circuits with strain-isolation layers and mesh layouts for high-performance electronics on fabric, vinyl, leather, and paper. *Adv. Mater.* **21**, 3703–3707 (2009).
- Heremans, P. et al. Mechanical and electronic properties of thin-film transistors on plastic, and their integration in flexible electronic applications. *Adv. Mater.* **28**, 4266–4282 (2015).
- Nam, S. H. et al. Highly sensitive non-classical strain gauge using organic heptazole thin-film transistor circuit on a flexible substrate. *Adv. Funct. Mater.* **24**, 4413–4419 (2014).
- Zeng, X. M., Lai, A., Gan, C. L. & Schuh, C. A. Crystal orientation dependence of the stress-induced martensitic transformation in zirconia-based shape memory ceramics. *Acta Mater.* **116**, 124–135 (2016).
- Barraza-Lopez, S., Fregoso, B. M., Villanova, J. W., Parkin, S. S. P. & Chang, K. Colloquium: physical properties of group-IV monochalcogenide monolayers. *Rev. Mod. Phys.* **93**, 011001 (2021).
- Hu, Z. et al. Recent progress in 2D group IV–IV monochalcogenides: synthesis, properties and applications. *Nanotechnology* **30**, 252001 (2019).
- Wu, M. & Zeng, X. C. Intrinsic ferroelasticity and/or multiferroicity in two-dimensional phosphorene and phosphorene analogues. *Nano Lett.* **16**, 3236–3241 (2016).
- Varotto, S. et al. Room-temperature ferroelectric switching of spin-to-charge conversion in germanium telluride. *Nat. Electron.* **4**, 740–747 (2021).
- Wang, C., You, L., Cobden, D. & Wang, J. Towards two-dimensional van der Waals ferroelectrics. *Nat. Mater.* **22**, 542–552 (2023).
- Seidel, J. et al. Conduction at domain walls in oxide multiferroics. *Nat. Mater.* **8**, 229–234 (2009).
- Choi, T., Lee, S., Choi, Y. J., Kiryukhin, V. & Cheong, S. W. Switchable ferroelectric diode and photovoltaic effect in BiFeO₃. *Science* **324**, 63–66 (2009).
- Absor, M. A. U. & Ishii, F. Intrinsic persistent spin helix state in two-dimensional group-IV monochalcogenide MX monolayers (M=Sn or Ge and X=S, Se, or Te). *Phys. Rev. B* **100**, 115104 (2019).
- Wang, H. & Qian, X. Giant optical second harmonic generation in two-dimensional multiferroics. *Nano Lett.* **17**, 5027–5034 (2017).

41. Rangel, T. et al. Large bulk photovoltaic effect and spontaneous polarization of single-layer monochalcogenides. *Phys. Rev. Lett.* **119**, 067402 (2017).
42. Cook, A. M., Fregoso, B. M., de Juan, F., Coh, S. & Moore, J. E. Design principles for shift current photovoltaics. *Nat. Commun.* **8**, 14176 (2017).

Publisher's note Springer Nature remains neutral with regard to jurisdictional claims in published maps and institutional affiliations.

Open Access This article is licensed under a Creative Commons Attribution-NonCommercial-NoDerivatives 4.0 International License, which permits any non-commercial use, sharing, distribution and

reproduction in any medium or format, as long as you give appropriate credit to the original author(s) and the source, provide a link to the Creative Commons licence, and indicate if you modified the licensed material. You do not have permission under this licence to share adapted material derived from this article or parts of it. The images or other third party material in this article are included in the article's Creative Commons licence, unless indicated otherwise in a credit line to the material. If material is not included in the article's Creative Commons licence and your intended use is not permitted by statutory regulation or exceeds the permitted use, you will need to obtain permission directly from the copyright holder. To view a copy of this licence, visit <http://creativecommons.org/licenses/by-nc-nd/4.0/>.

© The Author(s) 2025

¹Center for High Pressure Science, State Key Laboratory of Metastable Materials Science and Technology, Yanshan University, Qinhuangdao, China.

²National Laboratory of Solid State Microstructures, and Collaborative Innovation Center of Advanced Microstructures, Nanjing University, Nanjing, China. ³College of Engineering and Applied Sciences, and Jiangsu Key Laboratory of Artificial Functional Materials, Nanjing University, Nanjing, China.

⁴Center for X-Mechanics, School of Aeronautics and Astronautics, Zhejiang University, Hangzhou, China. ⁵These authors contributed equally: Chong Wang, Zeya Li, Yingchun Cheng. ✉ e-mail: xjweng@ysu.edu.cn; htyuan@nju.edu.cn; anmin@ysu.edu.cn

Methods

Fabrication of microscale GeSe samples for TEM tensile strain testing

GeSe single crystals were synthesized via the chemical vapour transport method⁴³. GeSe flakes for in situ TEM experiments under tensile strain were fabricated by using a focused ion beam (Helios G5, Thermo Fisher Scientific) as follows. First, a thin lamella was milled from as-grown crystals with the polished surface, and then it was cut and transferred onto a TEM half-grid fixed by Pt welding. Second, the lamella was laterally narrowed to a width of 3 μm and then further shaped into a nanobridge specimen with dimensions of 100–300 nm in width and 1–3 μm in length. The diamond gripper was specifically designed with a diamond indenter tip to grip the nanobridge specimen for tensile testing. The presence and orientation of the twins in the lamella were ascertained via TEM observation and corresponding electron diffraction analysis. A thin surface amorphous layer with a few nanometres thickness typically forms on the GeSe sample after focused ion beam milling, which has a minimal impact on the twinning-mediated superelasticity in GeSe owing to its minimal thickness and low mechanical properties (Supplementary Figs. 32–34).

In situ TEM and STEM characterization

In situ PTP tensile tests were performed with a positioning control of 0.1 nm in a custom-designed X-Nano TEM system⁴⁴. The in situ DT tensile experiments were conducted with a displacement loading rate of 1.0 nm s⁻¹ using a Hysitron PicoIndenter PI95 (Hysitron). The PTP method provides stability for applying strain to very thin samples, making it ideal for HRTEM measurements, while the DT method allows for direct stress–strain measurements. All in situ mechanical tests were performed in a JEM-ARM200F microscope (JEOL) at 200 kV. All STEM observations were performed in an aberration-corrected JEM-ARM300F2 (JEOL) at 300 kV with a 25 mrad probe convergence angle. HAADF images were captured by using 60–200 mrad inner-out collection angles. STEM imaging of the twin structures involved transferring the sample, mounted on the X-Nano stage, from the image-corrected JEM-ARM200F—where the twin domains were initially identified—to the probe-corrected JEM-ARM300F2. The sample was reloaded until the twin domains reappeared, and stress was maintained to stabilize them, enabling the capture of high-resolution images. The details of the in situ TEM and STEM characterizations can be found in Supplementary Information. Corresponding HAADF-STEM image simulation was conducted according to the experimental imaging parameters by using a developed software⁴⁵.

Density functional theory calculations

The structure and mechanical properties of *Pnma*-GeSe were simulated by using the projector-augmented wave⁴⁶ method as implemented in the VASP code⁴⁷. Generalized gradient approximation with the functional of Perdew, Burke and Ernzerhof⁴⁸ was adopted to treat the exchange–correlation energy. The energy barrier was calculated by the climbing-image nudged elastic band method⁴⁹. The model used for calculating the transition state is a $2 \times 2 \times 1$ supercell containing 32 atoms, as illustrated in Extended Data Fig. 6a. The dynamic evolution of GeSe under loading and unloading processes was simulated through alternative structure optimization and molecular dynamics. Strain along the zigzag direction is applied step-by-step on a periodic model containing 256 atoms in a cell, constructed using a transformation

matrix of $\begin{pmatrix} 2 & 2 & 0 \\ -8 & 8 & 0 \\ 0 & 0 & 1 \end{pmatrix}$ applied to the primitive cell, as shown in Extended

Data Fig. 6c. After relaxing the lattice and atom positions at each strain, AIMD at 300 K was carried out for at least 10 ps (time step of 1 fs, 10,000 steps) to check the dynamic stability. The canonical ensemble (NVT) with a Nosé–Hoover thermostat was used⁵⁰. If the structure was unstable and transformed to another configuration within the first 10 ps, a simulation with an additional 10 ps was run until the structure

stabilized. The structure, energy and stress of the final state are determined by averaging the atomic positions in the last 1 ps and re-relaxing the configuration. In the molecular dynamics simulation, an energy cut-off of 320 eV, a k -point of Γ and an energy convergence criterion of 10^{-6} eV were used. In relaxation, to obtain more accurate energy and stress data, an energy cut-off of 500 eV, a k -point resolution of $2\pi \times 0.04 \text{ \AA}^{-1}$, an energy convergence criterion of 10^{-6} eV and a force criterion of 0.01 eV \AA^{-1} were used. To determine the directional Young's modulus and Poisson's ratio, we calculated the elastic tensor of intrinsic GeSe by applying finite distortions to the lattice and deriving the elastic constants from the stress–strain relationship. This calculation was performed using the VASP code with the parameters IBRION = 6 and ISIF = 3. Subsequently, Young's modulus and Poisson's ratio as functions of the direction angle (θ) were obtained by applying a coordinate system transformation to the elastic tensor matrix.

Data availability

All data generated during the current study are available from the corresponding authors upon reasonable request. Additional datasets and videos are available on Materials Cloud⁵¹. Source data are provided with this paper.

References

- Liu, S. et al. Alloy engineered germanium monochalcogenide with tunable bandgap for broadband optoelectrical applications. *Phys. Rev. Mater.* **4**, 074012 (2020).
- Zhang, Y. et al. Atomic-scale observation of the deformation and failure of diamonds by in-situ double-tilt mechanical testing transmission electron microscope holder. *Sci. China Mater.* **63**, 2335–2343 (2020).
- He, D. S., Li, Z. Y. & Yuan, J. Kinematic HAADF-STEM image simulation of small nanoparticles. *Micron* **74**, 47–53 (2015).
- Blöchl, P. E. Projector augmented-wave method. *Phys. Rev. B* **50**, 17953–17979 (1994).
- Kresse, G. & Furthmüller, J. Efficient iterative schemes for ab initio total-energy calculations using a plane-wave basis set. *Phys. Rev. B* **54**, 11169–11186 (1996).
- Perdew, J. P., Burke, K. & Ernzerhof, M. Generalized gradient approximation made simple. *Phys. Rev. Lett.* **77**, 3865–3868 (1996).
- Henkelman, G., Uberuaga, B. P. & Jónsson, H. A climbing image nudged elastic band method for finding saddle points and minimum energy paths. *J. Chem. Phys.* **113**, 9901–9904 (2000).
- Hoover, W. G. Canonical dynamics: equilibrium phase-space distributions. *Phys. Rev. A* **31**, 1695–1697 (1985).
- Wang, C. et al. Additional datasets and videos underlying the manuscript: reversible shuffle twinning yields anisotropic tensile superelasticity in ceramic GeSe. *Mater. Cloud* <https://doi.org/10.24435/materialscloud:98-53> (2025).

Acknowledgements

This work was supported by the National Natural Science Foundation of China (grant numbers 52288102 (Y.T.), 52090022 (A.N.), 52025026 (X.-F.Z.), 92365203 (H.Y.) and 52072168 (H.Y.)), the Joint Funds of the National Natural Science Foundation of China (grant numbers U21A2086 (Z. Liu) and U24A6002 (H.Y.)) and the Hebei Natural Science Foundation (E2024203054 and E2022203109 (A.N.)).

Author contributions

C.W., Z. Li and Y.C. contributed equally to this work. Z. Liu, Y.T. and A.N. conceived the project and designed the experiments. C.W. and A.N. performed the GeSe nanodevice fabrication and TEM characterization. X.-J.W., X.-F.Z. and Y.C. performed the theoretical calculations. H.W. and Y.B. contributed to the mechanical testing support and finite element simulations. C.W., Z. Li, A.N., K.Z., T.X. and H.Y. analysed the data. Z. Li, A.N., H.Y. and Z. Liu wrote the paper with input from all authors.

Competing interests

The authors declare no competing interests.

Additional information

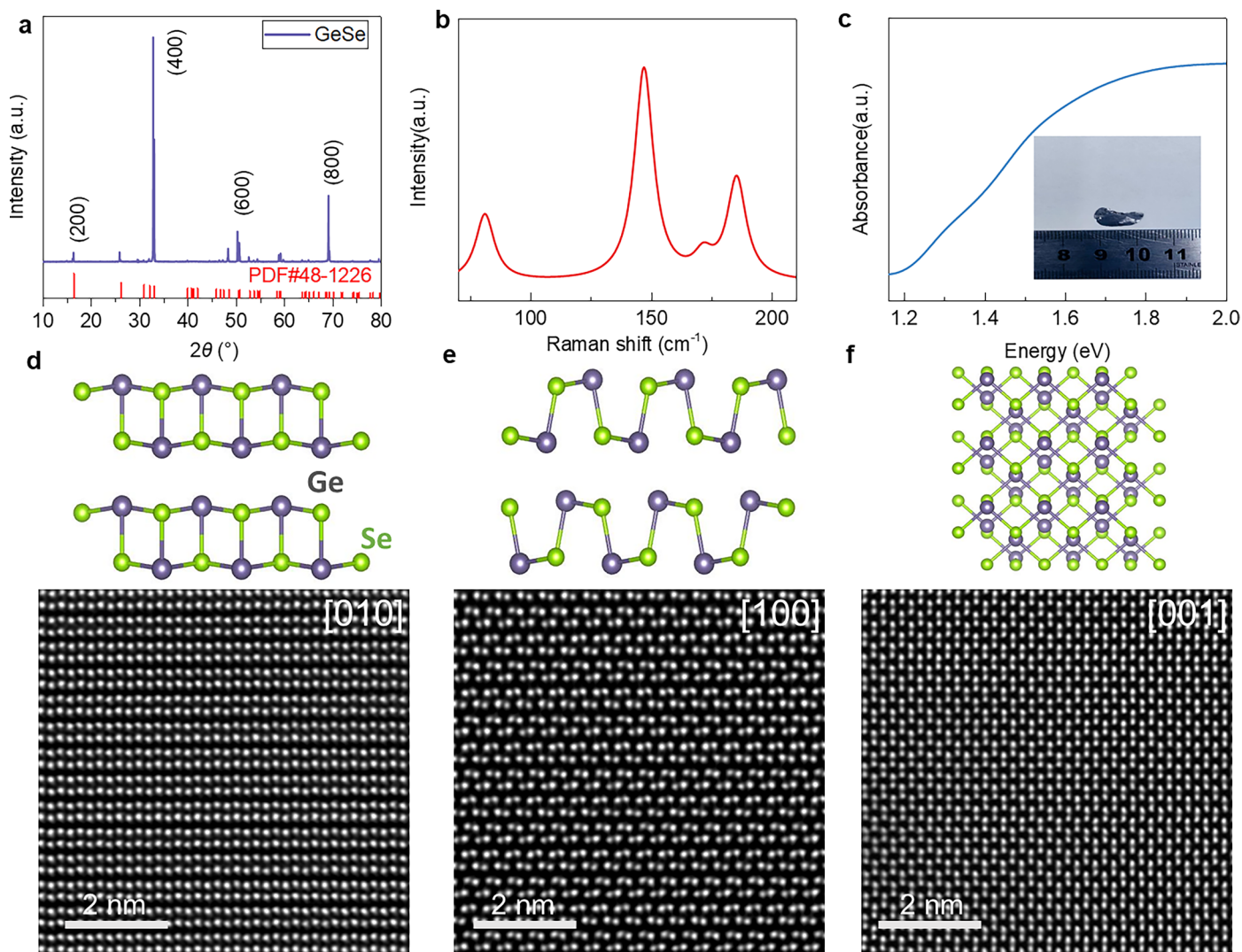
Extended data is available for this paper at <https://doi.org/10.1038/s41565-025-01902-7>.

Supplementary information The online version contains supplementary material available at <https://doi.org/10.1038/s41565-025-01902-7>.

Correspondence and requests for materials should be addressed to Xiao-Ji Weng, Hongtao Yuan or Anmin Nie.

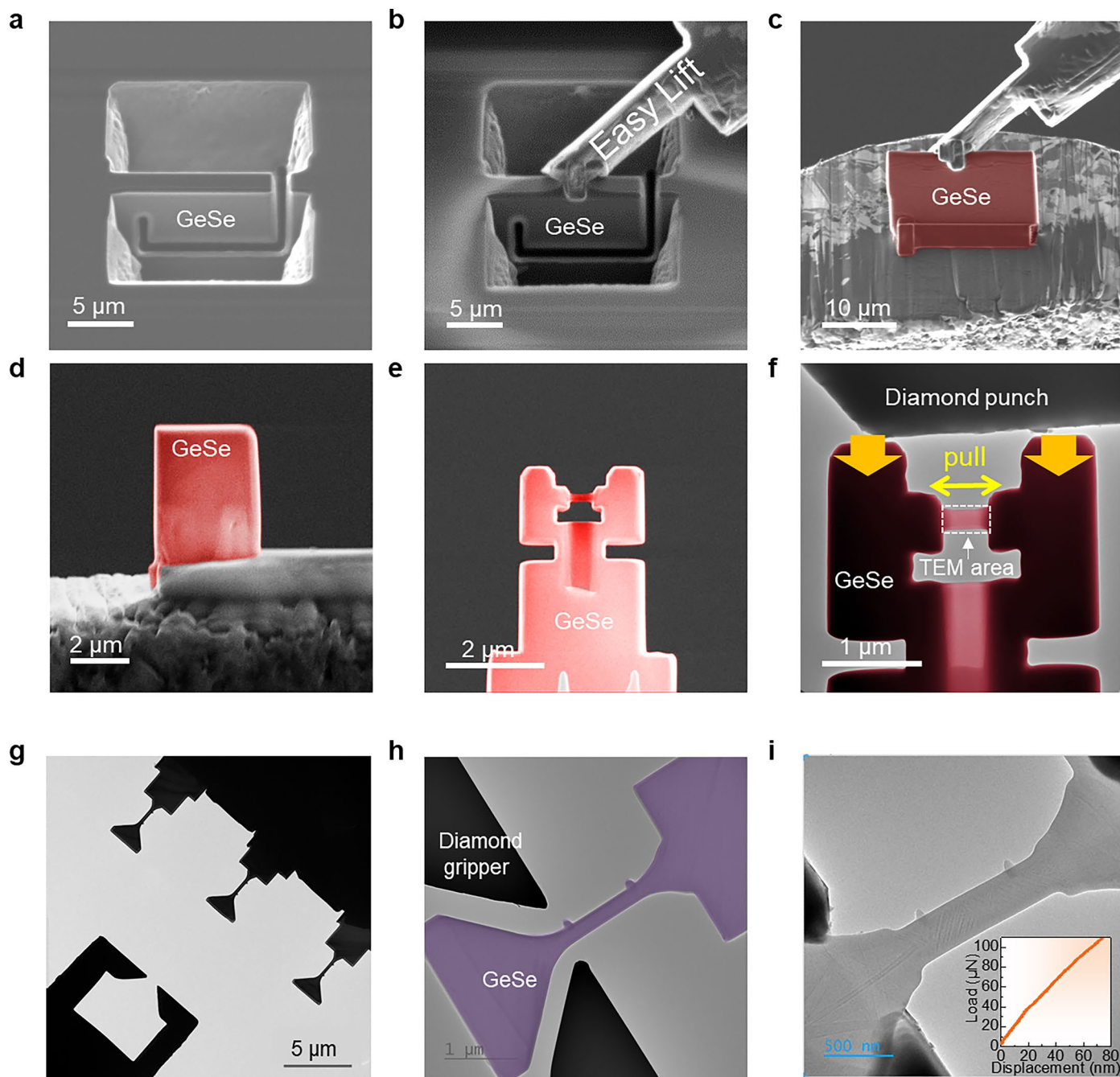
Peer review information *Nature Nanotechnology* thanks Qiang Guo, Andrej Ostapovec and Wu Zhou for their contribution to the peer review of this work.

Reprints and permissions information is available at www.nature.com/reprints.



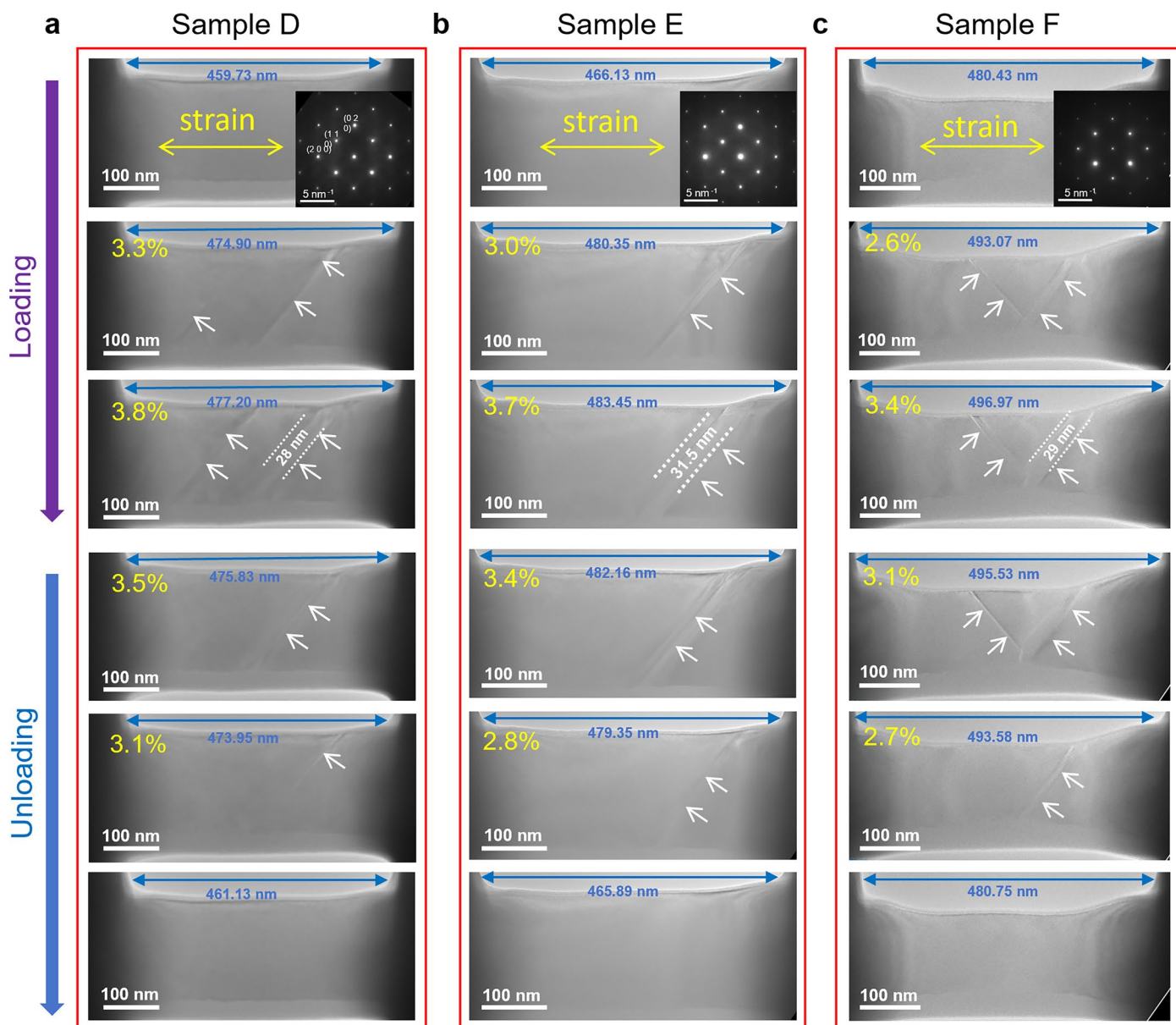
Extended Data Fig. 1 | Crystal structure and basic optical properties of the GeSe crystal. **a**, XRD pattern of the GeSe single crystal. The XRD pattern was obtained from the ground powder. The out-of-plane lattice constant c of 10.84 Å was obtained by using Bragg's law. **b**, Raman spectrum of the GeSe single crystal. The four observed peaks at 81, 147, 172 and 185 cm^{-1} , correspond to the A_g^1 , B_{3g} , A_g^2 and A_g^3 modes, which is consistent with the reported results for GeSe with space group $Pnma$. **c**, Absorption spectrum of the GeSe single crystal. The inset in (c)

shows an optical image of the as-grown GeSe single crystal. The optical bandgap of GeSe was determined to be around 1.2 eV, confirming the semiconducting nature of layered GeSe. **d-f**, Atomic crystal models (top panel) and HAADF-STEM images (bottom panel) of GeSe crystal along the [010], [100], and [001] orientations, respectively. In the model, Ge and Se atoms are colored in purple and green, respectively. From the STEM results, lattice constants can be determined as follows: $a = 3.81$ Å, $b = 4.38$ Å, and $c = 10.80$ Å.



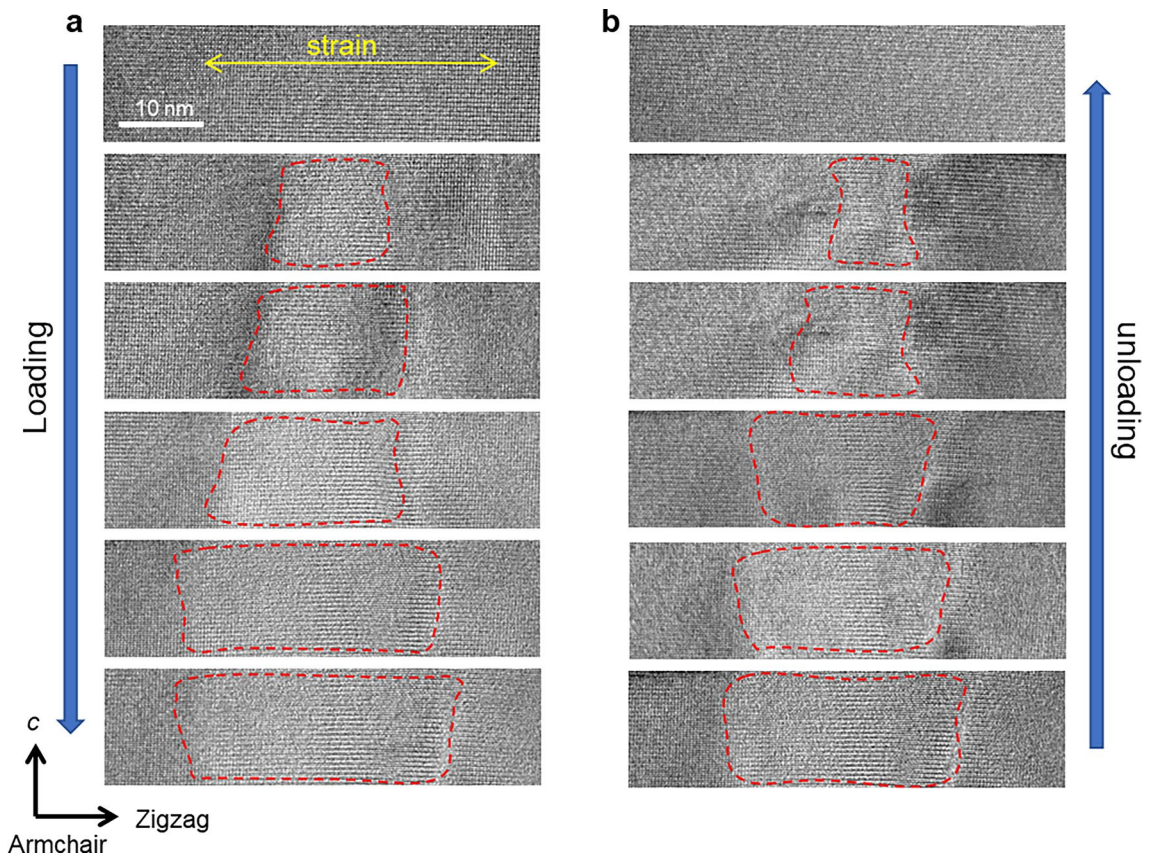
Extended Data Fig. 2 | Fabrication of GeSe samples for in-situ TEM tensile testing. **a–e**, SEM images showing the microfabrication process of the GeSe PTP device for tensile testing. **f**, TEM image of a PTP device to demonstrate the applied uniaxial tensile strain on the tiny bridge by pushing the convex pillars with a diamond punch. **g–i**, TEM images showing the microfabrication process of the GeSe nanobridge samples for direct tensile testing. **g**, TEM image showing

a series of GeSe nanobridges with a diamond gripper sculpted from a diamond indenter tip. **h**, Alignment of one tensile sample and the diamond gripper prior to straining. **i**, TEM image showing the formation of stripy domains in the nanobridge during strain loading. Inset is the collected load–displacement curve during the loading of strain along the zigzag direction.



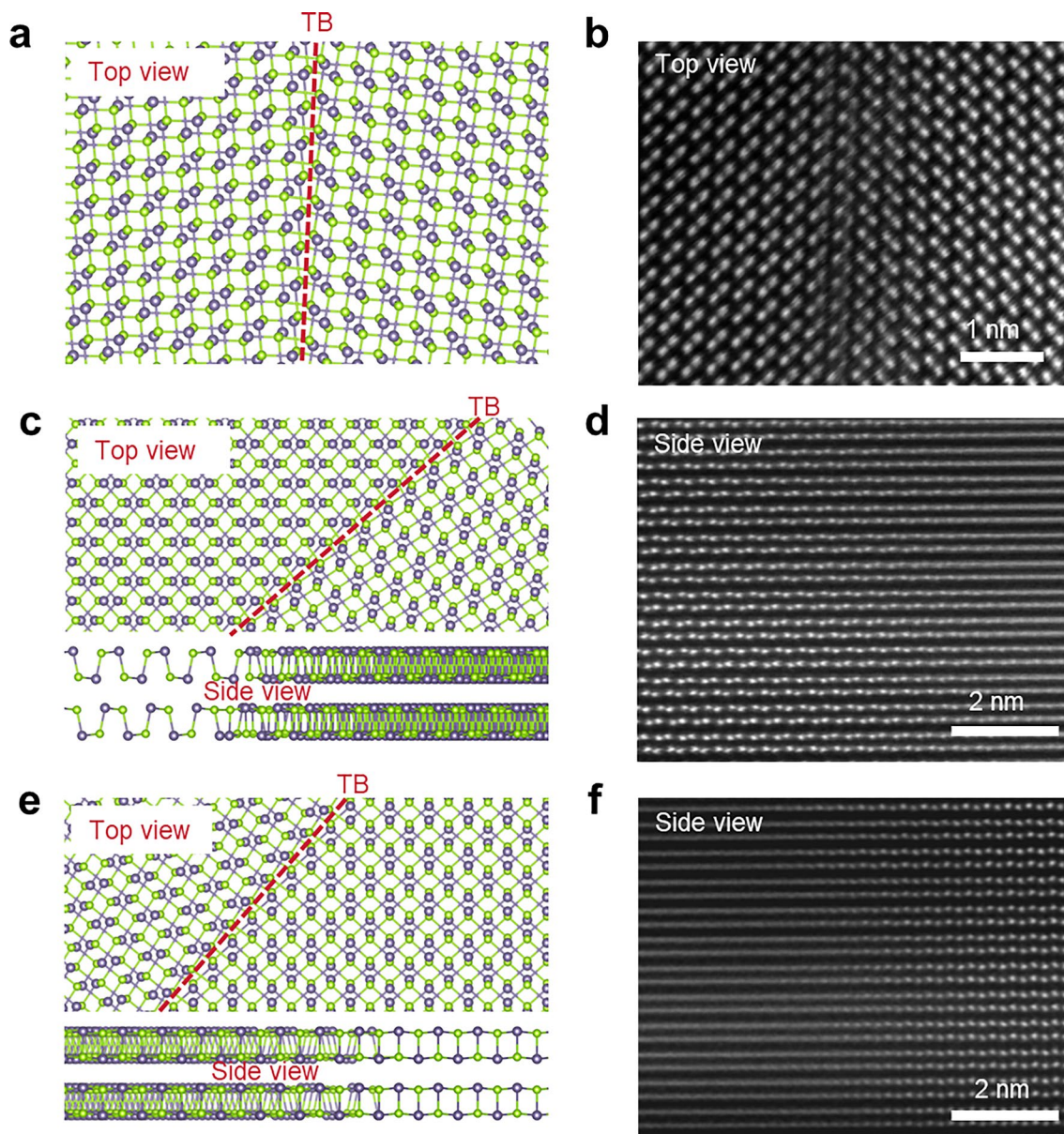
Extended Data Fig. 3 | Reproducibility of superelasticity along the zigzag direction. Three microfabricated GeSe samples were stretched along the zigzag direction *via* the PTP method. The orientation of each sample was determined with the SAED pattern inserted as the inset in the corresponding panel. The white arrows highlight the stripy domains formed under strain. In the two tested samples in (a, b), stripy domains are observed to be formed just along the $[110]$ direction, while in the tested sample in (c), stripy domains are found to appear along both the $[110]$ and $[\bar{1}\bar{1}0]$ directions. Since $[110]$ and $[\bar{1}\bar{1}0]$ are equivalent

crystal orientations in GeSe, we can conclude that the twin boundary prefers to form along the $\langle 110 \rangle$ direction. With increasing strain during the loading process, the stripy domains appear and gradually widen, while they gradually narrow and disappear with decreasing strain during the unloading process. Such a reversible process is repeatable after multiple loading and unloading strains, and the GeSe sample consistently exhibits superelastic behavior. These results indicate the high reproducibility of superelasticity in GeSe.



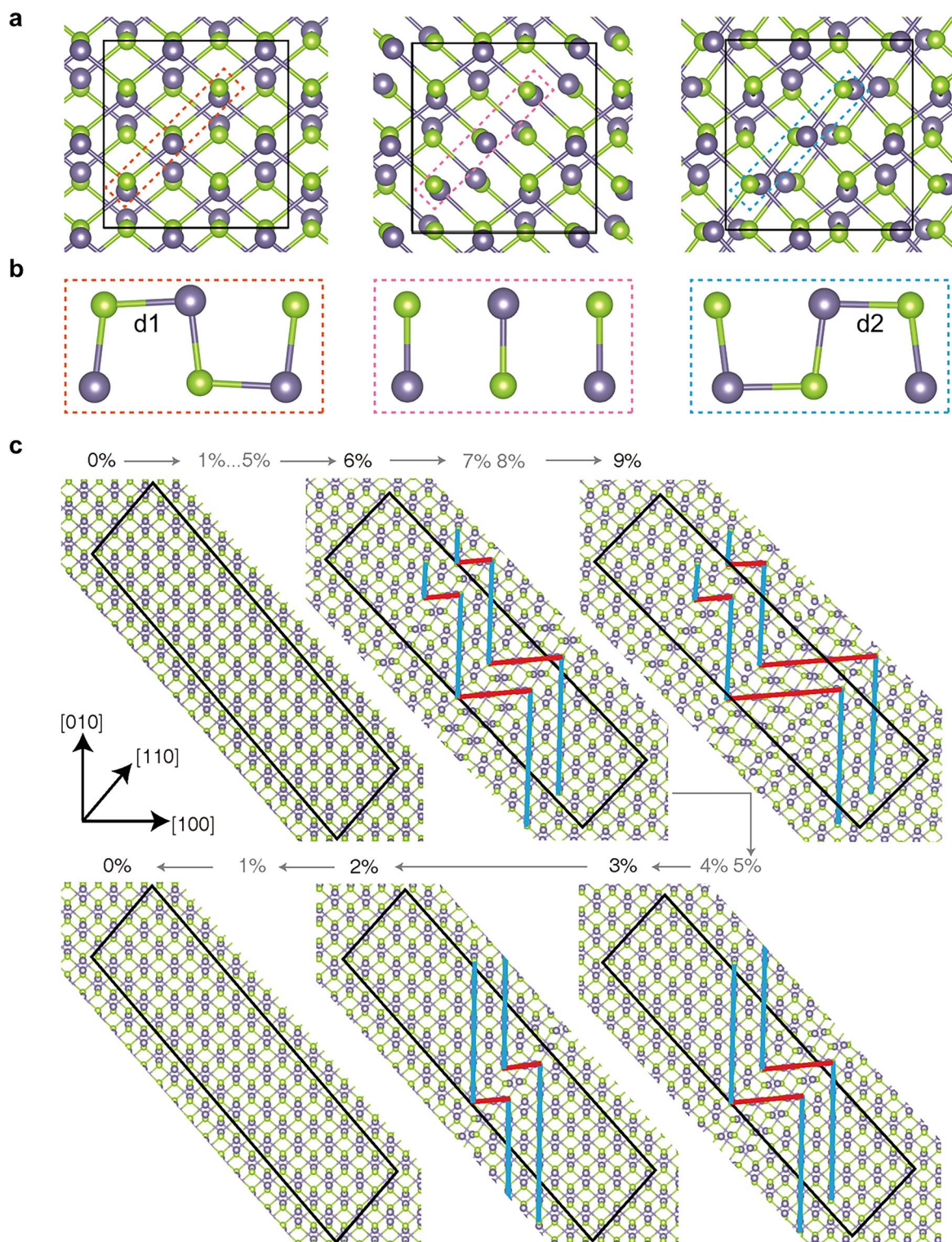
Extended Data Fig. 4 | In situ observation of superelastic behavior in GeSe along the armchair direction. HRTEM images of a GeSe sample (Sample G) under uniaxial strain along the zigzag direction during strain loading (**a**) and during unloading process (**b**) *via* the PTP method. The red dashed lines mark out the twin domain, which exhibits increases and decreases in width during

strain loading and unloading, respectively. This observation of strain-dependent domain dynamics further confirms the superelastic behavior of GeSe. The side view also reveals that superelastic behavior occurs throughout all the layers of the GeSe sample.



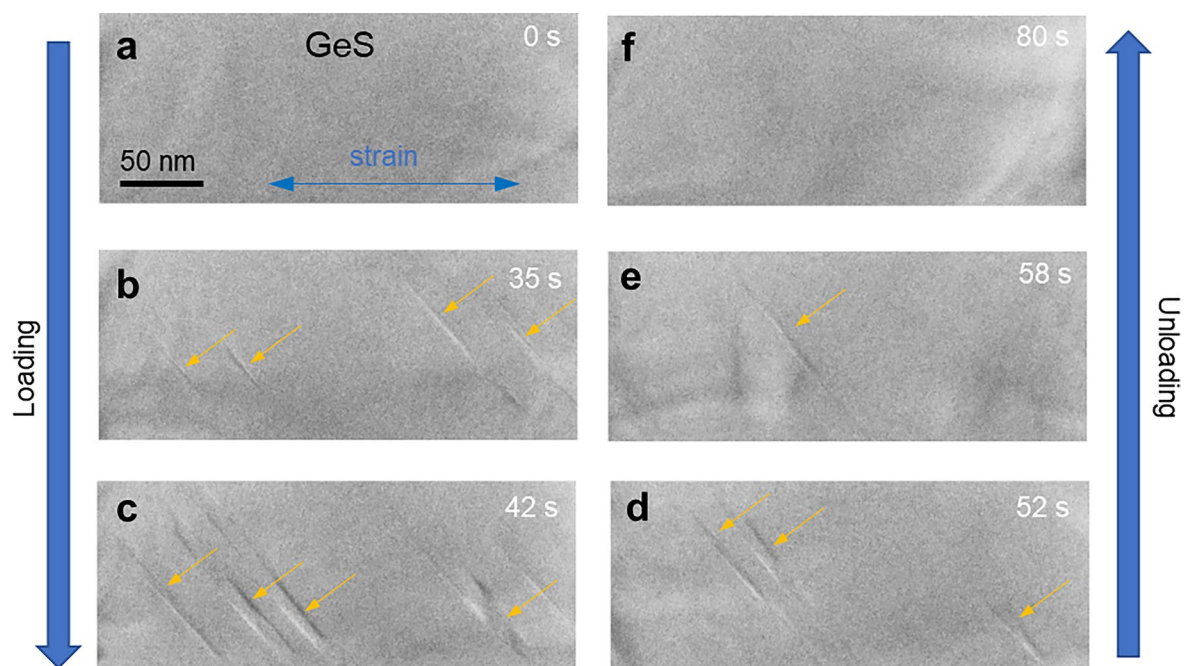
Extended Data Fig. 5 | Atomic-scale structure of the twin boundary in superelastic GeSe. **a**, Atomic structure and **(b)** HAADF-STEM image showing a top view of the twin boundary between the Matrix (right part) and twin domain (left part) along the $[001]$ zone axis (Sample B). **c**, Top and side views of the atomic structure of the twin boundary. The side view is along the $[100]$ zone axis in the twin domain (left part). **d**, HAADF-STEM image providing a side-view of the twin boundary along the $[100]$ zone axis in the twin domain

(left panel, Sample G). **e**, Top and side views of the atomic structure of the twin boundary. In comparison with **(c)**, the twin boundary is rotated about 7 degrees counterclockwise. The side view is along the $[010]$ zone axis in the Matrix (right part). **f**, HAADF-STEM image showing a side view of the twin boundary along the $[010]$ zone axis in the Matrix (right panel, Sample G). In the model, Ge and Se atoms are colored in purple and green, respectively.



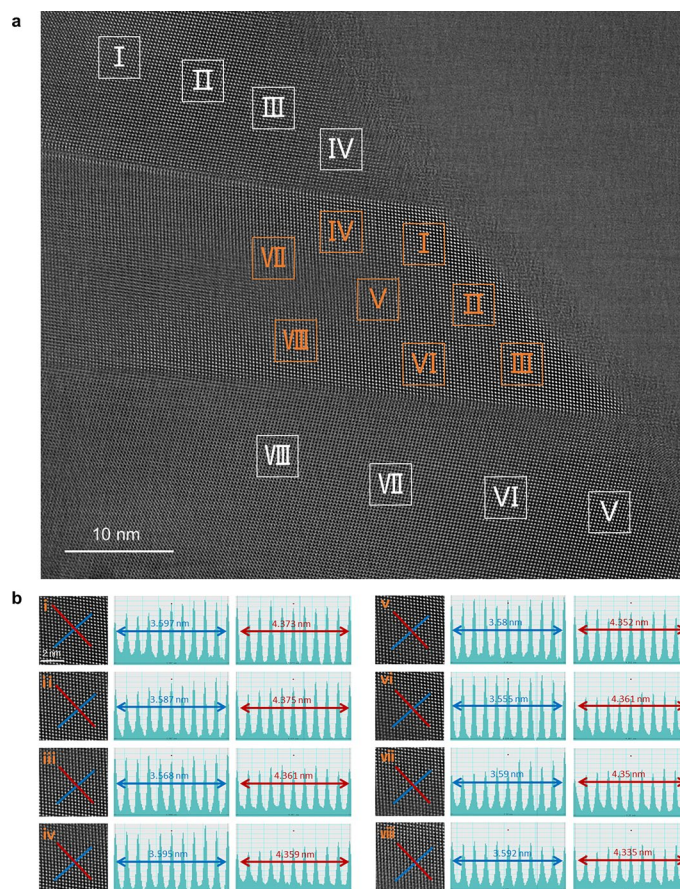
Extended Data Fig. 6 | Shuffle twinning of GeSe under tensile strain. a, The structure of GeSe before twinning (left), after twinning (right), and at the energy saddle point in the transformation pathway (middle) for a strain of 7% along the zigzag direction. Ge and Se atoms are colored in purple and green, respectively.

b, The local bond switching in the structures corresponding to (a). **c,** Structural evolution of the twin domains (marked by red lines) in the GeSe model during loading and unloading simulation, corresponding to the data points in Fig. 3b in the main text.



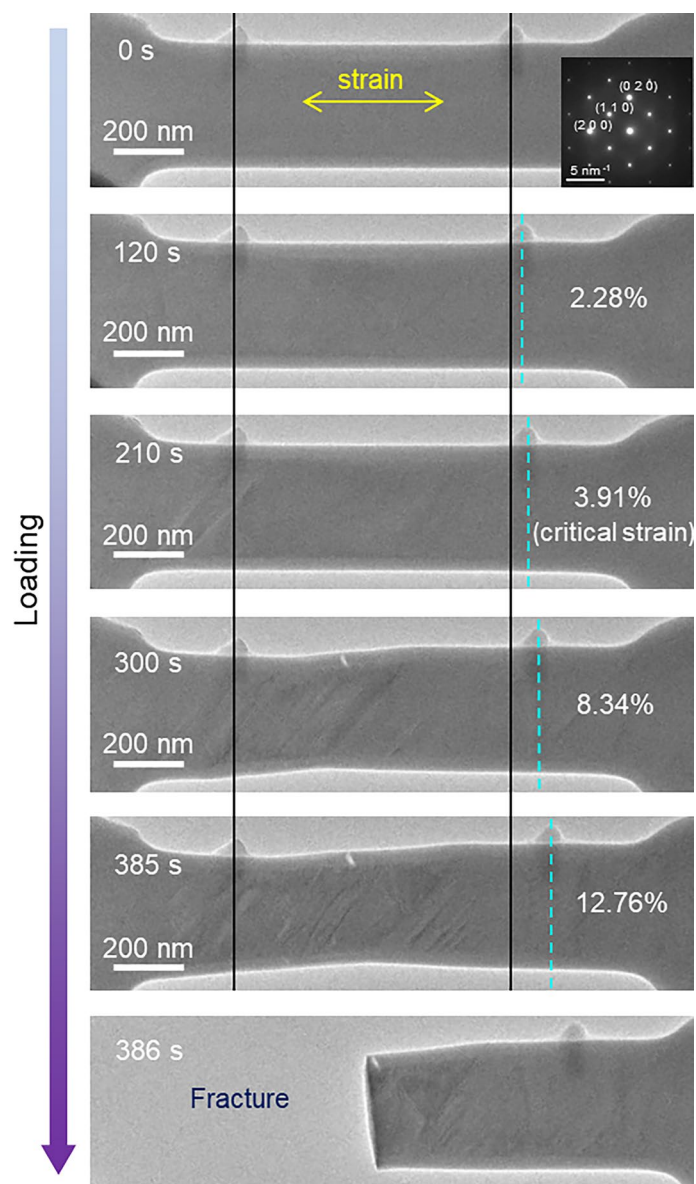
Extended Data Fig. 7 | Twinning-induced superelasticity in GeS along the zigzag direction. In-situ TEM images of the GeS sample during strain loading (a-c) and unloading (d-f) via the PTP method. The yellow arrows highlight the stripy domains formed under strain. One can clearly observe the generation and disappearance of the stripy domain in the GeS ceramic crystal during strain

loading and unloading. Such stripy domains are also found to form along the $\langle 110 \rangle$ direction. This result indicates that the shuffle twinning mechanism can serve as a general mechanism to induce superelasticity in those ceramic crystals with similar crystal structures.

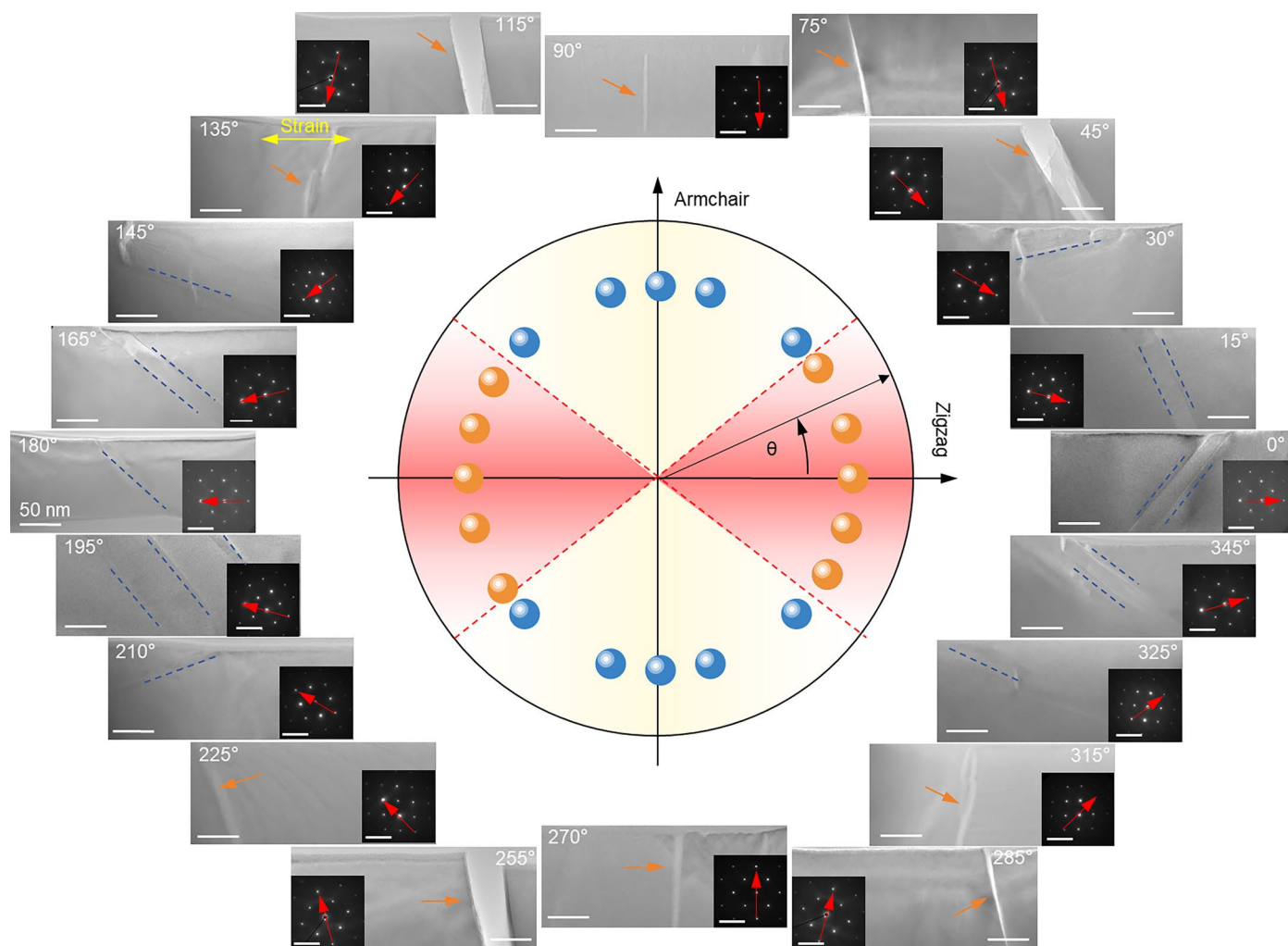


Extended Data Fig. 8 | Determination of the lattice parameters of GeSe under tensile strain. a, One extracted snapshot from an HRTEM video for a GeSe sample (Sample C) under tensile strain along zigzag direction. The white (orange) rectangles represent the eight randomly selected regions for lattice parameter determination in twin domain (Matrix). **b**, Determination of the lattice

parameters of GeSe in twin domain region. The blue and red solid lines represent the zigzag and armchair directions. In each selected region, ten unit cells were taken along the zigzag (middle panel) and armchair (right panel) directions for lattice parameter determination. The same approach is applied for the lattice parameter determination in Matrix region.



Extended Data Fig. 9 | In-situ TEM tensile testing on a GeSe sample along the zigzag direction *via* the DT method. The tested GeSe sample (Sample H) gradually elongated until fracture with increasing strain along the zigzag direction. Stripy domains began to appear at a critical strain of -3.91%, and a maximum strain as high as -12.76% was reached before fracture.



Extended Data Fig. 10 | Loading direction dependence of superelasticity in GeSe. The TEM images show typical fabricated GeSe samples for both the DT and PTP testing under a large strain with θ (θ is denoted as the angle between the zigzag direction and loading direction) ranging from 0 to 360° in steps of 15°. Insets are SAED patterns of the tested samples; the scale bar is 5 nm⁻¹. The zigzag direction of each sample is indexed by a red arrow, and the stripy domains generated due to tensile strain are highlighted by blue dashed lines. The orange arrows indicate fracture of the tested samples under a large strain. The schematic diagram in the center illustrates the range of tensile directions for the

appearance of superelasticity in GeSe. The balls represent the experimentally measured values of θ , among which the orange balls highlight the superelastic case and the blue balls highlight the elastic case. One can see that the fabricated PTP samples are able to exhibit observable stripy domains (indicative of superelasticity) only when θ lies in the range from 325° to 30° (or 145° to 210°). Otherwise, the GeSe samples show no sign of stripy domains until they are stretched to fracture during loading. This finding indicates that superelasticity is highly anisotropic in GeSe.